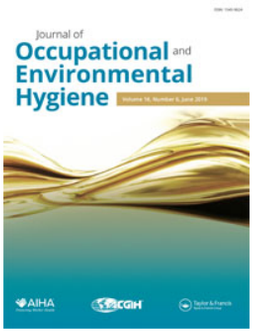

Taylor & Francis
Taylor & Francis Group

Journal of Occupational and Environmental Hygiene

ISSN: 1545-9624 (Print) 1545-9632 (Online) Journal homepage: https://www.tandfonline.com/loi/uoeh20

Size, composition, morphology, and health implications of airborne incidental metal-containing nanoparticles

Natalia I. Gonzalez-Pech, Larissa V. Stebounova, Irem B. Ustunol, Jae Hong Park, T. Renee Anthony, Thomas M. Peters & Vicki H. Grassian

To cite this article: Natalia I. Gonzalez-Pech, Larissa V. Stebounova, Irem B. Ustunol, Jae Hong Park, T. Renee Anthony, Thomas M. Peters & Vicki H. Grassian (2019) Size, composition, morphology, and health implications of airborne incidental metal-containing nanoparticles, Journal of Occupational and Environmental Hygiene, 16:6, 387-399, DOI: 10.1080/15459624.2018.1559925

To link to this article: https://doi.org/10.1080/15459624.2018.1559925

JOURNAL OF OCCUPATIONAL AND ENVIRONMENTAL HYGIENE
2019, VOL. 16, NO. 6, 387–399
https://doi.org/10.1080/15459624.2018.1559925

Taylor & Francis
Taylor & Francis Group

Size, composition, morphology, and health implications of airborne incidental metal-containing nanoparticles

Natalia I. Gonzalez-Pech[a], Larissa V. Stebounova[b], Irem B. Ustunol[c], Jae Hong Park[d], T. Renee Anthony[b], Thomas M. Peters[b], and Vicki H. Grassian[a,c,e]

[a]Department of Chemistry and Biochemistry, University of California San Diego, La Jolla, California; [b]Department of Occupational and Environmental Health, The University of Iowa, Iowa City, Iowa; [c]Department of Nanoengineering, University of California San Diego, La Jolla, California; [d]School of Health Sciences, Purdue University, West Lafayette, Indiana; [e]Scripps Institution of Oceanography, University of California San Diego, La Jolla, California

ABSTRACT

There is great concern regarding the adverse health implications of engineered nanoparticles. However, there are many circumstances where the production of incidental nanoparticles, i.e., nanoparticles unintentionally generated as a side product of some anthropogenic process, is of even greater concern. In this study, metal-based incidental nanoparticles were measured in two occupational settings: a machining center and a foundry. On-site characterization of substrate-deposited incidental nanoparticles using a field-portable X-ray fluorescence provided some insights into the chemical characteristics of these metal-containing particles. The same substrates were then used to carry out further off-site analysis including single-particle analysis using scanning electron microscopy and energy-dispersive X-ray spectroscopy. Between the two sites, there were similarities in the size and composition of the incidental nanoparticles as well as in the agglomeration and coagulation behavior of nanoparticles. In particular, incidental nanoparticles were identified in two forms: submicrometer fractal-like agglomerates from activities such as welding and supermicrometer particles with incidental nanoparticles coagulated to their surface, herein referenced as nanoparticle collectors. These agglomerates will affect deposition and transport inside the respiratory system of the respirable incidental nanoparticles and the corresponding health implications. The studies of incidental nanoparticles generated in occupational settings lay the groundwork on which occupational health and safety protocols should be built.

KEYWORDS

Fractal-like agglomerates; incidental nanoparticles; NP-collectors; respiratory deposition curve; single-particle analysis

Introduction

The health implications of engineered nanoparticles (ENPs) have been discussed for over a decade in the environmental health and safety (EHS) field.[1] Efforts to develop a framework for evaluating EHS implications of ENPs and the corresponding risk assessments are currently in progress.[2–4] These risk assessments are usually based on property-driven or functional assay-rooted approaches that consider changes in the properties of nanoparticles (NPs) under relevant environmental conditions.[5] However, these approaches are difficult to apply to incidental nanoparticles (INPs) – nanoparticles unintentionally generated as a side product of anthropogenic processes – because they are often poorly characterized.

In recent years, there has been great interest in assessing the concentrations of nanoparticles to which workers are exposed during ENP production and product development.[6,7] Such studies have resulted in correlations between higher concentrations with specific work activities[8,9] and enabled the development of methodologies to better assess ENPs in the workplace.[10–12] This work has undoubtedly helped to improve the occupational safety in nanotechnology industries.[13] However, the INPs generated in many occupations are not fully understood. Welding is one of the processes that generate high levels of INPs that are known to contain mostly iron (Fe) and manganese (Mn) oxides, among many other metals.[14] These particles are of great interest in terms of the health

CONTACT Vicki H. Grassian vhgrassian@ucsd.edu University of California San Diego, 9500 Gilman Drive, Mail Code 0314, 3030 Urey Hall Addition, La Jolla, 92093 California.

Color versions of one or more of the figures in the article can be found online at www.tandfonline.com/uoeh.

Supplemental data for this article can be accessed on the publisher's website. AIHA and ACGIH members may also access supplementary material at http://oeh.tandfonline.com/.

implications for welders due to the toxicity of Mn even at low levels of exposure.[15] Other activities, such as smelting[16,17] or surface treatment,[18] have been reported to generate significant quantities of aluminum (Al) containing INPs. In general, any industrial process that involves combustion or generation of metal fumes likely produce INPs.[19–21] It is therefore important to understand the nature of these INPs.

The health implications of airborne nanoparticles are not a new concern. For decades, epidemiological studies have associated particulate matter (PM) in air pollution with increases in mortality and the frequency of cardiovascular,[22–25] pulmonary,[26,27] and neurological diseases.[28–30] Despite the fact that mechanisms by which PM causes adverse health effects have not been fully elucidated, several studies have linked them to the ability to trigger oxidative stress.[23,25,31] Stronger associations of PM exposure with adverse health effects have been found for ultrafine particles, *i.e.,* nanoparticles in the ambient environment, rather than larger micron-sized particles.[24] This finding may be due in part to the fact that ultrafine particles possess a higher content of transition metals and organics than larger particles, making them prone to generate reactive oxygen species (ROS).[25,32] Furthermore, ultrafine particles are usually generated by anthropogenic sources such as power plants, car exhausts, combustion, mining, and other industrial sources.[30]

Recently, Maher et al.[33] observed anthropological magnetite nanoparticles, generated by combustion, in the brains of humans from Mexico and England. This study confirms that nanoparticles can translocate from the respiratory tract to accumulate in the brain after inhalation, a hypothesis once solely based on results of experiments in mice.[34–36] Moreover, sufficient accumulation occurs even at relatively low PM concentrations (with peak values for roadside dust at ~40 $\mu g/m^3$) that can result in a neurodegenerative disease.[33] This finding motivated a thorough characterization of ultrafine particles, which have shown elevated concentrations of transition metals.[37–40] These studies become really relevant considering magnetic INPs found in the brain contained traces of other transition metals including nickel (Ni), platinum (Pt), cobalt (Co), and possibly copper (Cu).[33]

Detailed size and composition characterization of INPs is required to better understand their potential implications. Off-site measurement techniques usually provide more detailed information regarding size and composition including lower detection and quantification limits; however, the implementation of on-site techniques not only decreases the time and cost of characterization compared with off-site analyses. Typical off-site analyses involve gravimetric analysis or digestion of samples deposited onto substrates.[41] These samples are collected on-site by aspirating a known volume of air through a substrate, in order to collect enough particle mass for further analyses. While methods for measuring particle concentrations and size distribution on-site are well established,[42] more detailed chemical analysis, including elemental analysis, on-site remains challenging. A rapid method to measure on-site the mass concentration of metal-containing PM by size and composition from 10 nm to 10 μm was recently reported.[43] This method uses a nano micro-orifice uniform-deposit impactor (nano-MOUDI) to collect and separate particles by size and a field-portable X-ray fluorescence (FP-XRF) to measure metal concentrations. By using this nondestructive technique, the nano-MOUDI substrates can be used further for single-particle analysis, including scanning electron microscopy (SEM), and energy-dispersive X-ray spectroscopy (EDS). A previous study demonstrated that single-particle analysis can be used to distinguish airborne engineered nanomaterials from incidental particles.[44]

The present study aims to characterize and compare the composition, size and morphology of PM smaller than 10 μm, with a special interest on the INPs generated in two occupational settings. These sites were selected due to the significant concentration of Fe, Mn, and Cu found during a recent assessment of INPs exposure levels.[45] A FP-XRF was employed for on-site chemical characterization of metal-containing aerosol.[43] An off-site single-particle analysis was then performed to characterize primary particle morphology, composition and agglomerate status of INPs found in these two settings. Implications of these findings and potential health effects are discussed.

Methods

Test sites and sampling equipment

A heavy vehicle machining and assembly center and an iron foundry were selected based on the similarities in the composition of particulate matter: Fe, Cu, and Mn that were detected in a preliminary study at both sites.[45] The machining center produces construction and forestry equipment. Metal and metal oxide PM including nanoparticles were generated by robotic and manual metal inert gas (MIG) welding as well as metal parts grinding at this site. The foundry

Table 1. Concentrations of metals for total, respirable, and NPM fractions of the collected particles in the machining center.

	Day 1			Day 2			Day 3		
Element	Collected, $\mu g/m^3$	Respirable, $\mu g/m^3$	NPM, $\mu g/m^3$	Collected, $\mu g/m^3$	Respirable, $\mu g/m^3$	NPM, $\mu g/m^3$	Collected, $\mu g/m^3$	Respirable, $\mu g/m^3$	NPM, $\mu g/m^3$
Mn	28.9	27.3	7.8	24.7	23.9	6.8	18.4	17.3	4.8
Fe	190.4	159.4	45.1	151.2	135.3	36.9	137.8	112.4	32.1
Cu	3.1	3.0	0.9	5.1	4.4	1.0	1.3	1.2	1.0
Total	222.4	189.8	53.8	181.1	163.6	44.7	157.4	134.9	37.3

The concentrations were calculated by adding concentration multiplied by the corresponding fraction of each of the nano-MOUDI stages. NPM: nanoparticulate matter; MOUDI: micro-orifice uniform-deposit impactor.

manufactures ductile iron and grey iron metal parts, where PM monitoring was carried out during metal melting, metal pouring and grinding operations. In both locations, sampling was performed during 3 days using a field sampling cart placed in multiple areas of interest as described in detail previously.[45]

Size-resolved analysis of the INPs was carried out using the nano-MOUDI (Model 125-R, MSP Corporation, Shoreview, MN). The nano-MOUDI was operated at 10 L/min with 13 greased polycarbonate (PC) substrates (0.2 µm, 47 mm, Sterlitech Corporation, Kent, WA) as previously reported.[45] A mixed cellulose ester (MCE) filter (0.8 µm, 47 mm, Zefon International, Inc., Ocala, FL) was used as a backup filter in the last nano-MOUDI stage. Table S1 (see online supplemental information) shows the particle size ranges that each stage collects. Particles were collected onto transmission electron microscopy (TEM) grids (200-mesh carbon coated Ni grid, 01840N-F, Ted Pella Inc., CA) with an electrostatic precipitator (ESPnano model 100, DASH Connector Technology, Inc., WA).

For the machining center, sampling was carried out 6 hr/day on average. Day 1 sampling occurred near a robotic welding area, Day 2 sampling was near a manual welding and grinding areas, and Day 3 sampling was between the manual and robotic welding areas. For both types of welding, an ER70S-3 wire was used; the material safety data sheet (MSDS) reports elemental concentrations of 95.31% Fe, 1.85% Mn, 0.5% Cu, 0.15% C, 1.15% Si, 0.035% S, 0.025% P, 0.15% Ni, 0.15% Cr, 0.03% V, and 0.15% Mo. In the foundry, sampling was carried out 8 hr/day on average. The field measurement cart was positioned in the grinding area on Day 1, and in the hot metal melting/pouring area for Days 2 and 3. Ductile iron was produced on the first 2 days, while grey iron was produced on the third day. Although exact alloy compositions were proprietary information, the alloys met specifications for American Society for Testing and Materials (ASTM) grey iron and ductile iron designations. With Fe as the matrix, base composition for grey iron may range from 3.0 to 3.5% C, 0.6 to 0.9% Mn, 1.3 to 1.8% Si, together with relatively minor components of P and S. Ductile iron base composition is expected to range from 3.0 to 4.0% C, 0.1 to 1.0% Mn, 1.8 to 3.0% Si, with also P and S as relatively minor components.

Elemental analysis

Nano-MOUDI substrates were measured on-site using a FP-XRF analyzer (Niton XL3t Ultra, Thermo Scientific, Waltham, MA) to determine metal composition and concentration in each stage as recently reported.[43] The FP-XRF thin-film (standard filter) mode was used to measure Mn, Fe, Cu and Zn in units of $\mu g/cm^2$. Results were then converted to mass concentration considering the volume of air passed through the nano-MOUDI and sampling area of each substrate. The results herein presented are metal concentrations only; total mass concentrations were not calculated as the specific chemical formulas were not determined.

During the off-site analysis, nano-MOUDI substrates were digested separately using a Microwave Reaction System (MARS 6, CEM Corporation, Matthews, NC) following the NIOSH method 7302.[41] After digestion, the samples were diluted with milliQ water to 2% HNO_3 solutions. Inductively coupled plasma-mass spectrometry (ICP-MS; iCAP RQ ICP-MS, Thermo Fisher Scientific, MA) analysis was carried out for more than 45 metals present in Complete Standard Solution 71A and Refractory Elements Standard Solution 71B, using an Internal Standard Solution 71D. All solutions are National Institute of Standards and Technology (NIST) certified reference materials purchased from Inorganic Ventures (Christiansburg, VA). Standards were diluted with 2% HNO_3 (Trace Metal Grade, Fisher Scientific LLC, Pittsburgh, PA) to concentrations between 0.5 and 500 µg/L from which a calibration curve was generated. Table S2 shows the Limit of Detection (LOD) and Limit of Quantification (LOQ) for the metals observed in higher concentration in the PC and MCE filters for both ICP-MS and FP-XRF. LOD was determined as 3σ above the mean

Table 2. Concentrations of metals for total, respirable, and NPM fractions of the collected particles in the foundry.

	Day 1			Day 2			Day 3		
Element	Collected, $\mu g/m^3$	Respirable, $\mu g/m^3$	NPM, $\mu g/m^3$	Collected, $\mu g/m^3$	Respirable, $\mu g/m^3$	NPM, $\mu g/m^3$	Collected, $\mu g/m^3$	Respirable, $\mu g/m^3$	NPM, $\mu g/m^3$
Al	7.4	1.5	0.1	14.7	2.6	0.2	14.0	2.1	0.1
Mn	2.3	0.3	0.0	3.6	0.8	0.1	16.1	8.2	1.3
Fe	326.1	35.2	2.2	156.3	29.5	3.2	444.9	101.3	10.9
Cu	0.5	0.0	0.0	0.9	0.7	0.1	1.2	0.6	0.1
Zn	0.3	0.0	0.0	8.8	6.9	2.4	7.4	4.3	0.6
Total	336.6	36.9	2.3	184.3	40.5	5.9	483.6	116.5	13.1

The concentrations were calculated by adding concentration multiplied by the corresponding fraction of each of the nano-MOUDI stages. NPM: nanoparticulate matter; MOUDI: micro-orifice uniform-deposit impactor.

blank signal, where σ represents the standard deviation of the blank signal. LOQ was calculated as mean blank signal plus 10σ.

Electron microscopy analysis

Particles collected on TEM grids were imaged by TEM (JEOL-1230, JEOL Ltd., Japan) and images were analyzed by ImageJ software (version 1.50i, NIH, Bethesda, MD). PC substrates from nano-MOUDI Stages 3, 5, 7, 9, and 11 collected during Day 1 at the machining center site and during Day 2 at the foundry site were analyzed by SEM. In order to minimize charging effects, the PC substrates were coated with Iridium (K575X Sputter Coater, Quorum Technologies Ltd, UK) for 7 sec with an 85 mA deposition current prior to the analysis. A Field Emission Scanning Electron Microscope FE-SEM (Zeiss Sigma 500, Carl Zeiss, Germany) was used for morphology characterization. An Apreo SEM (Thermo Scientific, Hillsboro, OR) was used for EDS analysis. EDS analysis was performed with Pathfinder X-ray microanalysis software (Thermo Scientific, USA).

Results

On-site versus off-site chemical characterization

Fe, Mn, and Cu were found in substantial concentrations during 3 days of analysis at both sites. A comparison between size-dependent concentration distributions detected by ICP-MS and FP-XRF for the machining center (Day 1) and the foundry (Day 2) are shown in Figure 1. These days were selected for comparison because higher concentrations of metals were detected in the nanosize range in comparison with the concentrations during the other 2 days. Similar results were obtained for both techniques on different days and are shown for in Figures S1 and S2 for the machining center and foundry, respectively.

In the case of the machining center (Figure 1a), the distribution shapes of the three metals were for the most part similar with both methods, FP-XRF or ICP-MS. Only minor differences were noticed between the techniques. One of the differences is that ICP-MS has greater sensitivity for Mn. In the case of Cu, the discrepancies observed in the distributions are because the concentrations are near the quantification limit of FP-XRF technique (Table S2).

For the foundry (Figure 1b), when metals are present in concentrations higher than the LOQ, there is a good agreement in the reported concentration by both techniques. However, some of the biggest discrepancies observed in Fe and Mn are in the first three stages, where the larger particles are deposited. One possible explanation for the lower concentrations measured by ICP-MS is that there was a loss of PM during sample handling and sample transport; which can be more significant for these stages where larger amounts were deposited at the foundry compared to other stages. In addition, Cu was not detected by FP-XRF in the stages where ICP-MS sees high concentrations of Cu. The Cu concentrations measured by ICP-MS are lower than the LOQ of FP-XRF. The high LOD and LOQ for Cu using FP-XRF (Table S2) are due to the detection of Cu in the PC substrates and the significant contribution from the holder.[43] Nonetheless, the shape of the distributions and the reported concentrations by FP-XRF overall agree with the results from ICP-MS for Fe in both sites. This agreement is also observed for Mn and Cu when they are found in concentrations higher than the LOQs such as observed in machining center (Figure 1a).

These results suggest that nano-MOUDI followed by FP-XRF analysis is a good initial method for fast, on-site characterization of the metals and corresponding concentrations in the field and may be used routinely in occupational settings and other indoor environments. When required, the LOD limitation of FP-XRF can be overcome by collecting samples for longer periods of time. ICP-MS can then be used to confirm FP-XRF results and for the analysis of smaller particles where the mass and concentrations are much lower.

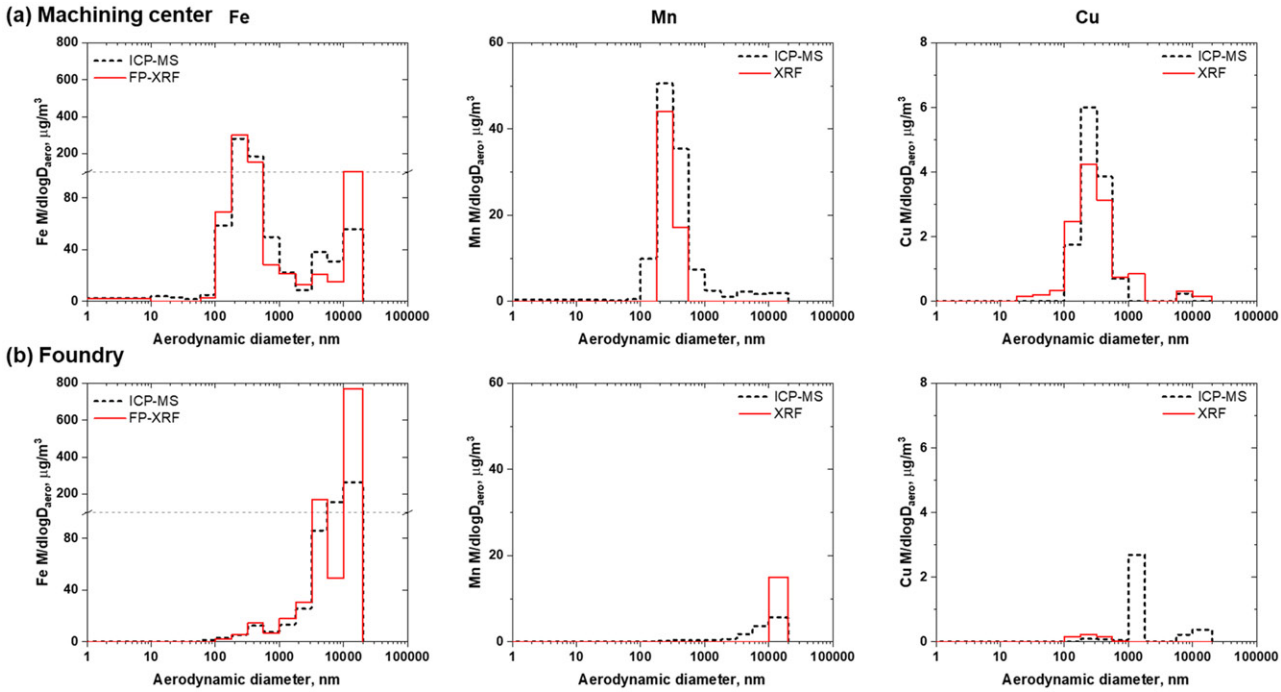

Figure 1. Comparison of the Fe (left), Mn (middle), and Cu (right) concentrations between on-site and off-site nano-MOUDI measurements at the machining center (a) and foundry (b). Fe concentrations are high for a few nano-MOUDI stages; therefore, a grid line at 100 µg/m^3 was added to mark a change in the scale dimensions.

Elemental characterization of incidental particles in two occupational settings

Figure 2a shows the mass concentrations of Mn, Fe, and Cu measured with ICP-MS in the machining center. The corresponding percentage of each element as a function of particle size is shown in Figure S3a for each day. Bimodal distributions are observed for most plots, with the exception of the Fe plot on Day 1 that shows Fe present in particles smaller than 100 nm (Figure 2a). The distribution between 100 to 1,000 nm agrees with what has been previously reported for the size distribution of particles in welding fumes.[14] This distribution represents the size of the agglomerates of nanoparticles. The second distribution, with a peak in the 10 µm size range, agrees with bigger particles reported in other studies of welding fumes.[46] In general, the distribution shapes of the three elements agree during the 3 days, where the highest concentration is in the nanoparticle-generated distribution (100–1,000 nm) with the exception of Cu during Day 2. The shift to a bigger size in the maximum value for Cu in the nanoparticles and the significant concentration (21%) in the substrate with a midpoint near 4.4 µm suggests an additional contribution of Cu. This is a reasonable explanation as Day 2 is the only day where the sampling cart was close to an area where another activity was occurring (grinding). In addition, the maximum percentage concentrations for Mn (17%) and Cu (3%) are in good agreement with the composition of the welding wires used at the site. The presence of Fe and Mn in stages that collected the smallest particles are observed in Day 1 and suggest that the size of primary particles is less than 10 nm. The detection of only Mn in Day 2 and Day 3 in the smallest size range suggests that the amount of INPs collected on Day 1 may be lower while total PM concentration (222.4 µg/m^3) is at least 22% higher than the other 2 days (181.1 µg/m^3 for Day 2 and 157.4 µg/m^3 for Day 3; Table 1).

A similar analysis was carried out for the foundry samples. In this site, many metal-generating processes were operating simultaneously, with a substantial proportion of the PM larger than the 20 μm upper limit of the sampling. The metal mass concentrations by size and sampling day measured with the nano-MOUDI are shown in Figure 2b. The percentage of each element in the corresponding substrate is shown in Figure S3b for each day. Compared with the machining center, mass concentrations were substantially higher and shifted to larger particle sizes at the foundry. Lower concentrations were also detected in the substrates collecting particles smaller than 1 µm. The mass concentrations of submicrometer particles were substantially lower in the grinding area (Day 1) than in the melt and pour areas (Days 2 and 3). Mass concentrations of nanoparticles were only detected

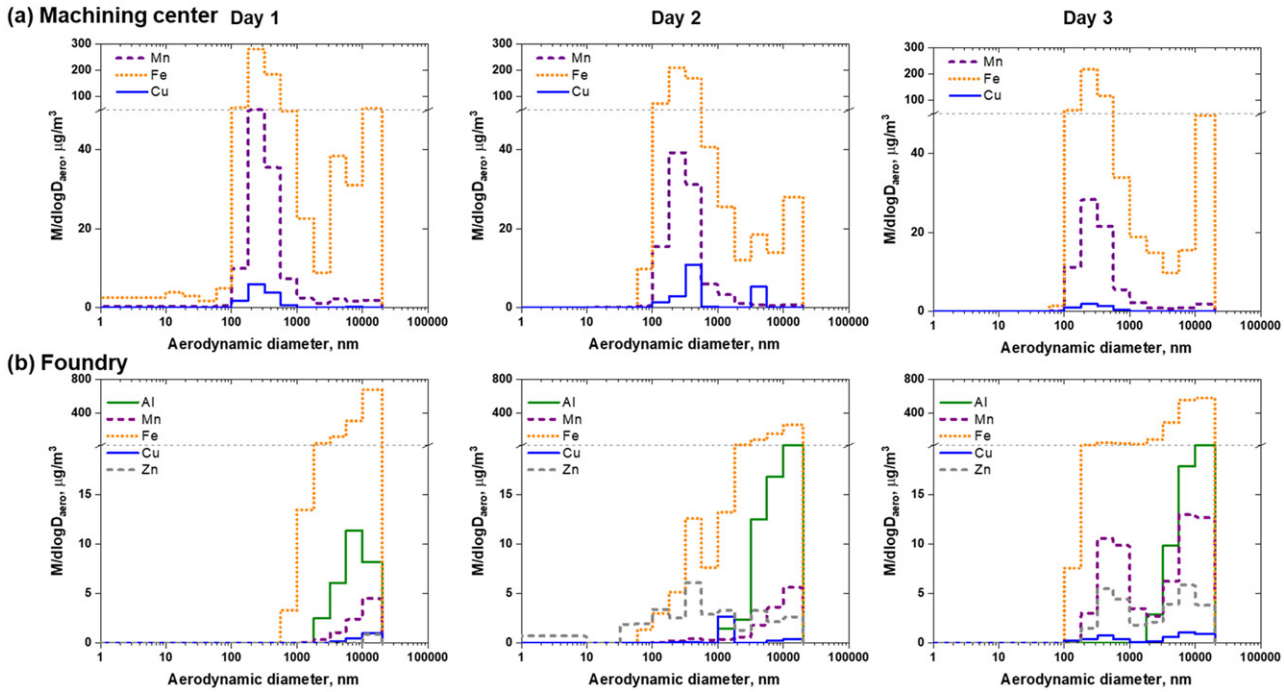

Figure 2. Mass concentration of the metals found in the elemental analysis using ICP-MS of each digested nano-MOUDI filters during Days 1, 2, and 3 at the machining center (a) and foundry (b) sites. Fe concentrations are high for a few nano-MOUDI stages; therefore, a grid line was added to mark a change in the scale dimensions at 50 µg/m^3 and 20 µg/m^3 for the (a) and (b), respectively.

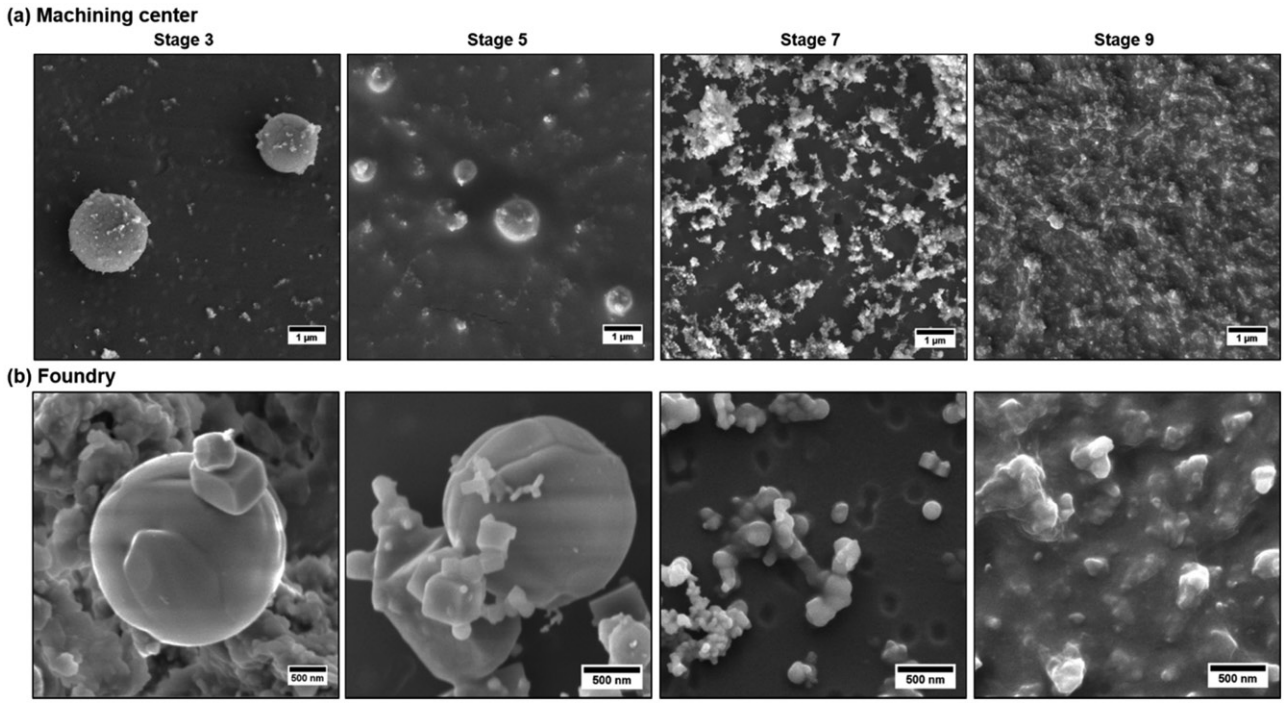

Figure 3. SEM images of particles found at the machining center and foundry sites for different size ranges including for particles collected by the nano-MOUDI Stages 3 (3.2–5.6 µm), 5 (1–1.8 µm), 7 (320–560 nm), and 9 (100–180 nm) at the machining center (a) and foundry (b).

during Day 2. Measurements in the metal melt and pour area show that the mass concentrations of submicrometer particles were substantially lower on Day 2 than on Day 3, which could relate to the different materials being produced (ductile iron on Day 2 and grey iron on Day 3). This explanation is supported by

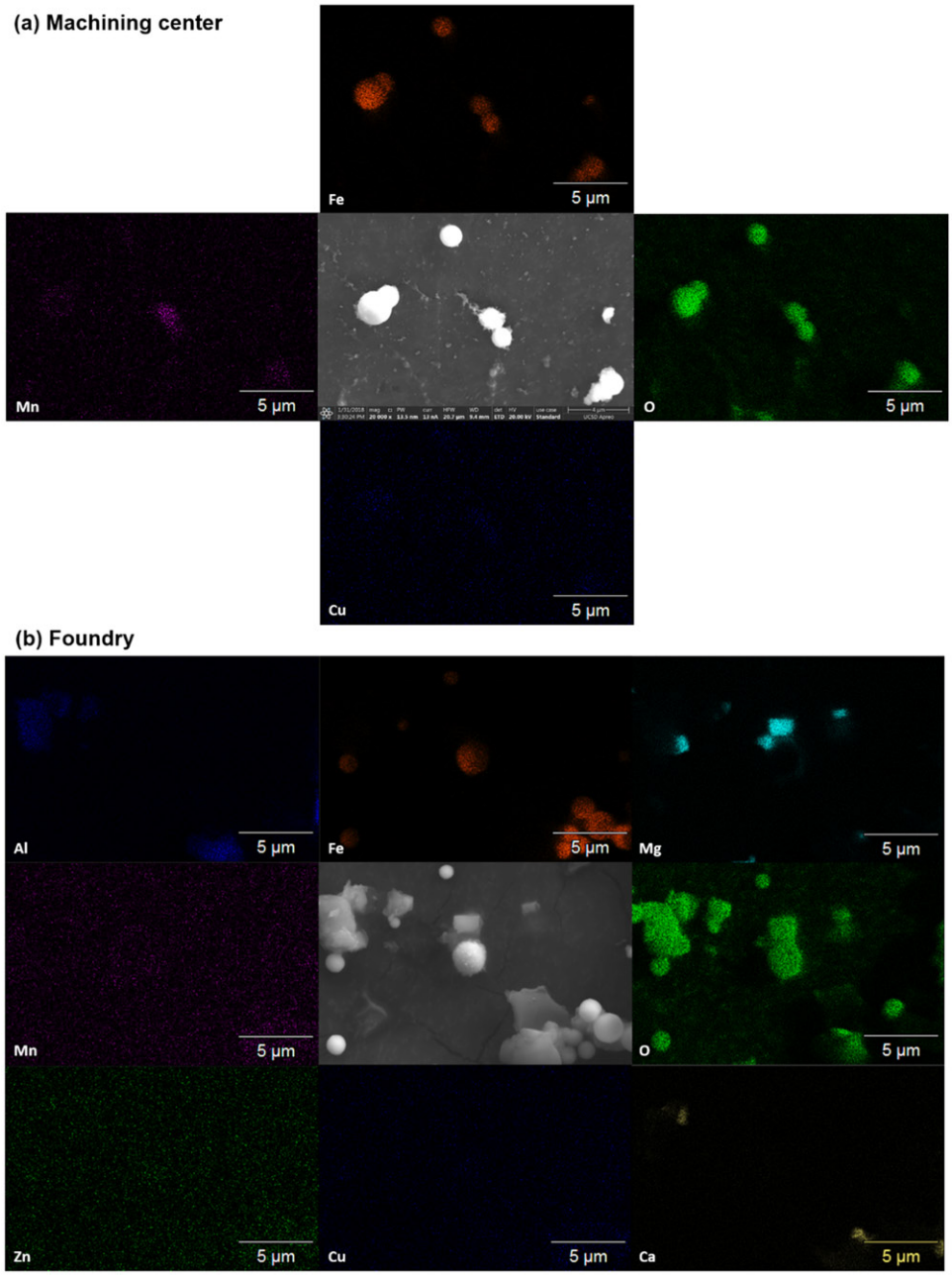

Figure 4. SEM-EDS of select micron-sized particles found in the machining center and foundry. SEM images are compared to the Fe, O, Mn, and Cu elemental mappings for both sites. Zn, Mg, Al, and Ca were also found and mapped in the foundry.

the fact that the metal composition differed by day. In the submicrometer range during Day 2, Fe relative concentration ranges between 46% and 70% (Figure S3). This is followed closely by Zn (27–53%), and Mn (1–3%) as a minor component. During Day 3, Fe is almost ten times more concentrated than on other days. Also, in the submicrometer range, Fe is the main component (74–95%) whereas Mn is present in a significant concentration as well (2–18%). This is followed closely by Zn (0–8%); Cu is only a minor component (Figure S3b). The differences in the mass concentrations and compositions of submicrometer particles between the three days are also evident in the respirable and the nanoparticulate matter (NPM) fractions (Table 2) of the particulate matter the workers are exposed to. Nanoparticle mass concentrations in the melt and pour areas (5.9 µg/m^3 for Day 2 and 13.1 µg/m^3 for Day 3, Table 2) were more than double than those in the grinding area (2.3 µg/m^3, Day 1 in Table 2). The composition of the melted metal has also an impact in the respirable fractions, which is 40.5 µg/m^3 for ductile iron on Day 2 and 116.5 µg/m^3 for grey iron on Day 3.

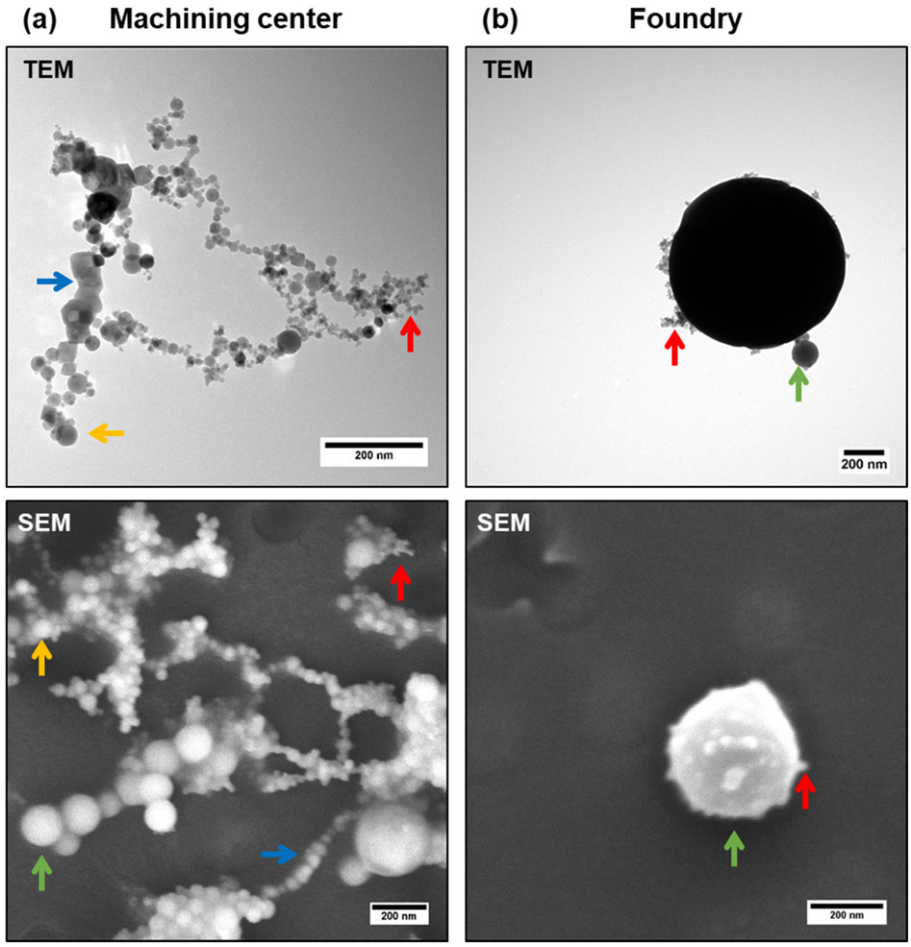

Figure 5. TEM (top) and SEM (bottom) images of particles detected at the machining center (a) and foundry (b) sites. For both sites, particles with different morphologies are observed including spherical and cubic (blue arrows) nanoparticles. At least four populations of spherical particle are observed including: very small nanoparticles, less than 10 nm (red arrows); small nanoparticles, less than 100 nm (yellow arrows); larger nanoparticles, approximately 100 nm (green arrows); and very larger particles that are hundreds of nanometers in size or micrometers in size (purple arrows).

Single-particle analysis of incidental particles in two occupational settings

To further characterize the morphology of the particles, five nano-MOUDI stages collected during Day 1 at the machining center, were selected for SEM analysis: Stage 3 (3.2–5.6 μm), Stage 5 (1.0–1.8 μm), Stage 7 (320–560 nm), Stage 9 (100–180 nm) and Stage 11 (32–59 nm). However, due to the diminished amount of the nanoparticles little data were obtained for Stage 11.

Figure 3a shows SEM images of the Stages 3, 5, 7, and 9. Low magnification images display the substrate homogeneity in-Figure S4a. Spherical micron-sized particles are observed on Stage 3. These large spherical particles have smaller particles deposited onto their surface. Smaller spheres with similar morphology are also observed in Stage 5. The expected submicrometer fractal-like agglomerates densely pack Stages 7 and 9. The shapes of small agglomerates are distinguishable in Stage 7 but not in Stage 9, due to the fact that an iridium thin film covered a very compact bed of nanoparticles.

For the foundry, Day 2 was selected for imaging due to the detection of metals in the stages collecting nanoparticles. Figure S4b shows low magnification SEM images of the Stages 3, 5, 7, and 9 from iron foundry to display the substrate homogeneity. Highly irregular agglomerates are present in Stages 3 to 7. Images obtained for Stage 7, where their concentration diminishes, show that these agglomerates are partially formed by a few hundred nanometers prisms. The images of Stages 3 and 5 show that spherical micron-sized particles are embedded in a dense layer of irregular agglomerates. In addition, in Stages 5 and 7, few fractal-like agglomerates are observed connecting some distant isolated particles. Figure 3b shows higher magnification SEM images to closely observe the morphology of the collected particles. Similar to

the other site, these micron-sized particles observed in Stages 3 and 5 have coagulated smaller particles on their surface, which have different shapes and sizes. On Stage 7, three kinds of particles are clearly detected: spheres with diameters around 150 nm, quasi-spherical nanoparticles with diameters around 30 nm and cubes with around 100 nm edges. On Stage 9, like in the previous site, the SEM images provide no morphology insights due to the iridium thin layer covering a very compact bed of nanoparticles.

To further understand the composition of the samples, SEM/EDS was carried out. Figure 4a shows the elemental mapping of some Fe-based micron-sized spheres found in Stage 3. The high association of O indicates these particles are Fe (hydroxy-)oxides, which is in agreement with previous reports for ambient, supermicrometer Fe-containing spheres possible from steel production.[47] The Mn mapping shows higher intensities for the fractal-like agglomerates located on the surface of the micron-sized spheres. Cu mapping provides little information since Cu concentrations detected by the ICP-MS are lower than 1%, which is below the detection limit of EDS.[48] Figure S5a shows a similar analysis for the particles collected in Stage 7, where large agglomerates (320–560 nm) of small nanoparticles are collected. In this case, the figure is less clear as the nanoparticles are smaller than the pixel size (40 nm), making the analysis less precise. However, key information is provided: (i) all nanoparticles contain oxygen; (ii) even when the Mn and Fe are easiest to be seen in the larger agglomerates, the areas with high intensity for each of these elements do not overlay; and (iii) although Cu mapping is not very clear, there are a few points with high intensity. These observations allow the following conclusion: most of the nanoparticles are either Mn, Fe, or Cu oxides but are probably not mixed metals oxides.

Figure 4b shows the elemental mapping of particles collected on Stage 3 in the foundry. For this stage, micron-sized spheres are seen to be composed of Fe and O whereas Mn, Cu, and Zn mappings do not show much signal and suggest their mass concentrations were below the limit of detection of EDS.[48] Aluminum is detected for the larger irregular agglomerates. This agrees with measured Al detected by ICP-MS (Figure S3b). Mg and Ca were also detected. In particular, Ca was observed when high Al was present. The presence of Ca, Al, and Si (not measured) is possibly related to the use of clay materials for the casting process.[49] MgO seems to be the main component of the micron-sized well-defined prisms, due to the presence of only Mg and O in those particles. The detection of Mg can also be attributed to clay materials but another source of Mg is as an additive in the preparation of ductile iron.[50] Figure S5b shows similar results for particles collected on Stage 7. Despite the fact that some nanoparticles are smaller than the pixel size (40 nm), key information can still be obtained: (i) most particles are oxides, as O it is observed in all the area where the SEM image shows particles; (ii) Mn and Cu are not observed as expected from the elemental analysis by ICP-MS; (iii) Mg is observed in large amount but is present on the agglomerates with a smooth surface; (iv) Fe is observed when small nanoparticles are observed; and (v) Zn mapping is not very clear, but there are a few points with high intensity which may indicate that some small particles are ZnO.

In general, metal oxide INPs were observed occurring with two distinct and specific morphologies: fractal-like agglomerates and NP-collectors, referring to the micron-sized spheres decorated with nanoparticles on their surface. The term NP-collector is inspired by the analogous deposition of nanoparticles on grains during their transport through porous media.[51] Figure 5 shows both morphologies observed with TEM (top) and SEM (bottom) in both sites. In the machining center, fractal-like agglomerates were more common and were formed by four kinds of nanoparticles: spherical particles with diameters ~200 nm (green arrows), ~50 nm (yellow arrows), and ~10 nm (red arrows); and cubic particles with edges ~70 nm edges (blue arrows). This kind of agglomerates is the main component of the PM found in the machining center, but the NP-collectors significantly contribute to the micron-sized particles. In contrast, in the foundry the fractal-like agglomerates were observed in a minor proportion, due to the small amount of mass found for nanoparticles. The NP-collector architecture was not only found in micron-sized spheres as shown in the top of Figure 5b, but also in ~200 nm particles shown at the bottom. The NP-collector architecture is in agreement with what had been modeled for the first stages of coagulation in particles where the size distribution is highly polydispersed.[52] However, these agglomerates are composed by two size distributions of primary particles. These agglomerates will likely follow the self-conserving size distribution observed for other aerosols,[53] including the fractal-like agglomerates observed in this work.

Discussion

A recent inhalation exposure study indicated that the sizes of both the agglomerates and the primary

particles are important in terms of pulmonary effects,[54] but our study suggest that composition and morphology of agglomerates might play a role in the route of deposition and translocation. Both fractal-like agglomerates and NP-collectors are inhalable particles, however the NP-collectors will have different penetration range and mechanism for deposition than the fractal-like agglomerates, and therefore, potentially different locations, types, and severities of health effects.

Small micron-sized particles (1–10 μm), such as the NP-collectors, have a high deposition efficiency in the nasal area.[55] This is of particular importance as the olfactory route is one of the proposed mechanisms for nanoparticle translocation to the brain.[36] Despite that in the studies modeling nasal deposition only a few micron-sized particles deposit on the olfactory region,[56] the NP-collectors could play an important role in nanoparticles translocation to the brain as their surface is enriched with multiple INPs. In addition, the translocation is expected to only occur for individual or a few nanoparticles agglomerates; which in both cases implies a de-agglomeration process. This de-agglomeration process could be promoted by the presence of biomolecules,[57] which are in high concentration and of diverse nature in the olfactory mucosa.[58]

On the other hand, the submicron fractal-like agglomerates are more likely to reach the alveolar region of the lungs. To estimate the deposition of those particles, the NPM criterion was developed: it represents the fraction of particles smaller than 300 nm that would deposit in the respiratory system of an average adult under light exercise and nose-breathing conditions.[59] The NPM criterion, designed to represent deposition of near-spherical nanoparticles, can be adjusted for different particle morphologies using an appropriate dynamic shape factor.[54] Tables 1 and 2 summarize the total concentrations collected by the nano-MOUDI, by element and day, and the corresponding respirable and dynamic NPM fractions for the machining center and the foundry, respectively. A significant proportion of the INPs found in the fractal-like agglomerates contribute to the NPM fraction. This means that the NPM fraction provides a good estimation of the fractal-like agglomerates that deposits in the respiratory system and may better reflect their adverse health effects.

Another important feature to consider is the heterogeneous composition of these agglomerates. Our EDS results suggest that both kinds of agglomerates are composed of single metal oxide particles, which is explained by the fact that each metal condenses at a different temperature.[60] Recent studies have shown that heterogeneous aggregation changes the fate of nanoparticles in the environment, as aggregation can change the reactivity of the nanoparticles including their ROS generation capabilities and photocatalytic properties.[61–63] Furthermore, the presence of Mn in Fe-rich PM has shown to change the proportion of the different oxidation states of Fe oxides.[40] This can have a significant effect on the inflammatory responses that the agglomerates will generate in the lung as each oxide dissolves at different rates.[64,65] In addition, the transport of the same INPs to different parts of the respiratory tract may generate different health effects.[66] For example, ZnO and Cu/CuO nanoparticles have shown to dissolve in the lung mostly by macrophage action,[64,67] but there is no indication that dissolution will occur if transported directly to the brain by the olfactory system. Previously, the generation of Fe and Mn nanoparticles was simulated to have a close model to characterize the materials and their behavior under contact with biological solutions.[65,68] However, from this study, it is concluded that new models that include heterogeneous agglomerates of incidental nanoparticles (Fe-Mn-Cu and Fe-Mn-Zn) with both architectures are required to better understand the health implications that these incidental nanoparticles will have.

Conclusions

In this work, an on-site technique was used successfully to analyze metals in PM collected with the nano-MOUDI. The same substrates were then used in off-site analysis to obtain more information of the collected particles, including morphology using SEM. Two types of agglomerates were found: fractal-like agglomerates, typically observed in INPs generating activities such as welding, and NP-collectors. Similar NP-collectors were recently observed in factories conducting MIG welding[46] and in PM collected from air pollution,[37] which indicates that they might be as common as the fractal-like agglomerates and should be studied in detail since they transport incidental nanoparticles on their surface.

Acknowledgments

The ICP-MS analysis was performed in the Environmental Complex Analysis Laboratory on the UC San Diego campus. Irem B. Ustunol also acknowledges Turkey's Ministry of National Education for her graduate fellowship and support.

Funding

This work was performed in part at the San Diego Nanotechnology Infrastructure (SDNI) of UCSD, a member of the National Nanotechnology Coordinated Infrastructure, which is supported by the National Science Foundation (Grant ECCS-1542148). This work utilized the TEM in the University of Iowa Central Microscopy Research Facilities that was purchased with funding from the NIH SIG grant number 1 S10 RR018998-01. This work used equipment borrowed from the University of Iowa Environmental Health Sciences Research Center, NIEHS/NIH P30 ES005605, a center funded by the National Institute of Environmental Health Sciences. Financial support for this work was provided by National Institute for Occupational Safety and Health grants R01 OH010238 and R01 OH010295.

ORCID

Natalia I. Gonzalez-Pech http://orcid.org/0000-0003-4189-850X
Larissa V. Stebounova http://orcid.org/0000-0002-1223-8492
Jae Hong Park http://orcid.org/0000-0003-0772-0433
T. Renee Anthony http://orcid.org/0000-0002-3780-7436
Thomas M. Peters http://orcid.org/0000-0002-1698-8856
Vicki H. Grassian http://orcid.org/0000-0001-5052-0045

References

[1] **Yokel, R.A., and R.C. MacPhail**: Engineered nanomaterials: Exposures, hazards, and risk prevention. *J. Occup. Med. Toxicol. 6(7)*:1–27 (2011).

[2] **Boyes, W.K., B.L.M. Thornton, S.R. Al-Abed, et al.**: A comprehensive framework for evaluating the environmental health and safety implications of engineered nanomaterials. *Crit. Rev. Toxicol. 47(9)*:767–810 (2017).

[3] **Mattsson, M.O., and M. Simko**: The changing face of nanomaterials: Risk assessment challenges along the value chain. *Regul. Toxicol. Pharmacol. 84*:105–115 (2017).

[4] **Grassian, V.H., A.J. Haes, I.A. Mudunkotuwa, et al.**: NanoEHS - Defining fundamental science needs: No easy feat when the simple itself is complex. *Environ. Sci.: Nano 3*:15–27 (2015).

[5] **Hendren, C.O., G.V. Lowry, J.M. Unrine, and M.R. Wiesner**: A functional assay-based strategy for nanomaterial risk forecasting. *Sci. Total Environ. 536*:1029–1037 (2015).

[6] **Brouwer, D.**: Exposure to manufactured nanoparticles in different workplaces. *Toxicology 269(2-3)*:120–127 (2010).

[7] **Curwin, B., and S. Bertke**: Exposure characterization of metal oxide nanoparticles in the workplace. *J. Occup. Environ. Hyg. 8(10)*:580–587 (2011).

[8] **Kuhlbusch, T.A.J., C. Asbach, H. Fissan, D. Gohler, and M. Stintz**: Nanoparticle exposure at nanotechnology workplaces: A review. *Part. Fibre Toxicol. 8(22)*:1–18 (2011).

[9] **Ding, Y., T.A.J. Kuhlbusch, M. Van Tongeren, et al.**: Airborne engineered nanomaterials in the workplace—A review of release and worker exposure during nanomaterial production and handling processes. *J. Hazard. Mat. 322*:17–28 (2017).

[10] **Park, J.H., I.A. Mudunkotuwa, L.W.D. Mines, T.R. Anthony, V.H. Grassian, and T.M. Peters**: A granular bed for use in a nanoparticle respiratory deposition sampler. *Aerosol Sci. Technol. 49(3)*:179–187 (2015).

[11] **Mines, L.W.D., J.H. Park, I.A. Mudunkotuwa, T.R. Anthony, V.H. Grassian, and T.M. Peters**: Porous polyurethane foam for use as a particle collection substrate in a nanoparticle respiratory deposition sampler. *Aerosol Sci. Technol. 50(5)*:497–506 (2016).

[12] **Asbach, C., C. Alexander, S. Clavaguera, et al.**: Review of measurement techniques and methods for assessing personal exposure to airborne nanomaterials in workplaces. *Sci. Total Environ. 603*:793–806 (2017).

[13] **Ham, S., S. Kim, N. Lee, et al.**: Comparison of nanoparticle exposure levels based on facility type—Small-scale laboratories, large-scale manufacturing workplaces, and unintended nanoparticle-emitting workplaces. *Aerosol Air Qual. Res. 15(5)*:1967–1978 (2015).

[14] **Berlinger, B., N. Benker, S. Weinbruch, et al.**: Physicochemical characterisation of different welding aerosols. *Anal. Bioanal. Chem. 399(5)*:1773–1780 (2011).

[15] **Baker, M.G., S.R. Criswell, B.A. Racette, et al.**: Neurological outcomes associated with low-level manganese exposure in an inception cohort of asymptomatic welding trainees. *Scand. J. Work Environ. Health. 41(1)*:94–101 (2015).

[16] **Thomassen, Y., W. Koch, W. Dunkhorst, et al.**: Ultrafine particles at workplaces of a primary aluminium smelter. *J. Environ. Monitor. 8(1)*:127–133 (2006).

[17] **Weinbruch, S., N. Benker, K. Kandler, et al.**: Morphology, chemical composition and nanostructure of single carbon-rich particles studied by transmission electron microscopy: source apportionment in workroom air of aluminium smelters. *Anal. Bioanal. Chem. 408(4)*:1151–1158 (2016).

[18] **Santos, R.J., and M.T. Vieira**: Assessment of airborne nanoparticles present in industry of aluminum surface treatments. *J. Occup. Environ. Hyg. 14(3)*:D29–D36 (2017).

[19] **Ono-Ogasawara, M., F. Serita, and M. Takaya**: Distinguishing nanomaterial particles from background airborne particulate matter for quantitative exposure assessment. *J. Nanopart. Res. 11(7)*:1651–1659 (2009).

[20] **Elihn, K., and P. Berg**: Ultrafine particle characteristics in seven industrial plants. *Ann. Occup. Hyg. 53(5)*:475–484 (2009).

[21] **Bemer, D., R. Regnier, I. Subra, B. Sutter, M.T. Lecler, and Y. Morele**: Ultrafine particles emitted by

flame and electric arc guns for thermal spraying of metals. *Ann. Occup. Hyg. 54(6)*:607–614 (2010).

[22] **Robertson, S., and M.R. Miller**: Ambient air pollution and thrombosis. *Part. Fibre Toxicol. 15(1)*:1–16 (2018).

[23] **Araujo, J.A., and A.E. Nel**: Particulate matter and atherosclerosis: Role of particle size, composition and oxidative stress. *Part. Fibre Toxicol. 6(24)*:1–19 (2009).

[24] **Hoek, G., R.M. Krishnan, R. Beelen, et al.**: Long-term air pollution exposure and cardio-respiratory mortality: A review. *Environ. Health. 12(43)*:1–15 (2013).

[25] **Rao, X.Q., J.X. Zhong, R.D. Brook, and S. Rajagopalan**: Effect of particulate matter air pollution on cardiovascular oxidative stress pathways. *Antioxid. Redox Signaling 28*:797–818 (2017).

[26] **Vignal, C., M. Pichavant, L.Y. Alleman, et al.**: Effects of urban coarse particles inhalation on oxidative and inflammatory parameters in the mouse lung and colon. *Part. Fibre Toxicol. 14(46)*:1–13 (2017).

[27] **Meldrum, K., C. Guo, E.L. Marczylo, T.W. Gant, R. Smith, and M.O. Leonard**: Mechanistic insight into the impact of nanomaterials on asthma and allergic airway disease. *Part. Fibre Toxicol. 14(45)*:1–35 (2017).

[28] **Pope, C.A., and D.W. Dockery**: Health effects of fine particulate air pollution: Lines that connect. *J. Air Waste Manag. Assoc. 56(6)*:709–742 (2006).

[29] **Ruckerl, R., A. Schneider, S. Breitner, J. Cyrys, and A. Peters**: Health effects of particulate air pollution: A review of epidemiological evidence. *Inhalation Toxicol. 23(10)*:555–592 (2011).

[30] **Heal, M.R., P. Kumar, and R.M. Harrison**: Particles, air quality, policy and health. *Chem. Soc. Rev. 41(19)*:6606–6630 (2012).

[31] **Cheng, H., A. Saffari, C. Sioutas, H.J. Forman, T.E. Morgan, and C.E. Finch**: Nanoscale particulate matter from urban traffic rapidly induces oxidative stress and inflammation in olfactory epithelium with concomitant effects on brain. *Environ. Health Perspect. 124(10)*:1537–1546 (2016).

[32] **Cassee, F.R., M.E. Heroux, M.E. Gerlofs-Nijland, and F.J. Kelly**: Particulate matter beyond mass: Recent health evidence on the role of fractions, chemical constituents and sources of emission. *Inhalation Toxicol. 25(14)*: 802–812 (2013).

[33] **Maher, B.A., I.A.M. Ahmed, V. Karloukovski, et al.**: Magnetite pollution nanoparticles in the human brain. *Proceed. Nat. Acad. Sci. 113(39)*:10797–10801 (2016).

[34] **Calderon-Garciduenas, L., B. Azzarelli, H. Acuna, et al.**: Air pollution and brain damage. *Toxicol. Pathol. 30(3)*:373–389 (2002).

[35] **Dorman, D.C., K.A. Brenneman, A.M. McElveen, S.E. Lynch, K.C. Roberts, and B.A. Wong**: Olfactory transport: A direct route of delivery of inhaled manganese phosphate to the rat brain. *J. Toxicol. Environ. Health-Part A 65(20)*:1493–1511 (2002).

[36] **Oberdorster, G., Z. Sharp, V. Atudorei, et al.**: Translocation of inhaled ultrafine particles to the brain. *Inhalation Toxicol. 16(6-7)*:437–445 (2004).

[37] **Gonzalez, L.T., F.E.L. Rodriguez, M. Sanchez-Dominguez, et al.**: Determination of trace metals in TSP and PM2.5 materials collected in the metropolitan area of Monterrey, Mexico: A characterization study by XPS, ICP-AES and SEM-EDS. *Atmosph. Res. 196*:8–22 (2017).

[38] **Jelenska, M., B. Gorka-Kostrubiec, T. Werner, et al.**: Evaluation of indoor/outdoor urban air pollution by magnetic, chemical and microscopic studies. *Atmos. Pollut. Res. 8(4)*:754–766 (2017).

[39] **Yang, Y., M. Vance, F.Y. Tou, A. Tiwari, M. Liu, and M.F. Hochella**: Nanoparticles in road dust from impervious urban surfaces: distribution, identification, and environmental implications. *Environ. Sci.-Nano 3(3)*:534–544 (2016).

[40] **Sanderson, P., S.S. Su, I.T.H. Chang, et al.**: Characterisation of iron-rich atmospheric submicrometre particles in the roadside environment. *Atmos. Environ. 140*:167–175 (2016).

[41] **Ashley, K.**: "Elements by ICP (microwave digestion), method 7302". NIOSH Manual of Analytical Methods (NMAM), 2016. Available at https://www.cdc.gov/niosh/docs/2014-151/pdfs/methods/7302.pdf (accessed May 9, 2018).

[42] **Amaral, S.S., J.A. de Carvalho, M.A.M. Costa, and C. Pinheiro**: An overview of particulate matter measurement instruments. *Atmosphere 6(9)*:1327–1345 (2015).

[43] **Park, J.H., I.A. Mudunkotuwa, K.J. Crawford, T.R. Anthony, V.H. Grassian, and T.M. Peters**: Rapid analysis of the size distribution of metal-containing aerosol. *Aerosol Sci. Technol. 51(1)*:108–115 (2017).

[44] **Peters, T.M., S. Elzey, R. Johnson, et al.**: Airborne monitoring to distinguish engineered nanomaterials from incidental particles for environmental health and safety. *J. Occup. Environ. Hyg. 6(2)*:73–81 (2009).

[45] **Stebounova, L.V., N.I. Gonzalez-Pech, J.H. Park, T.R. Anthony, T.M. Peters, and V.H. Grassian**: Particle concentrations in occupational settings measured with a Nanoparticle Respiratory Deposition (NRD) sampler. *Ann. Work Exposure Health 65(6)*:699–710(2018).

[46] **Stanislawska, M., T. Halatek, M. Cieslak, et al.**: Coarse, fine and ultrafine particles arising during welding - Analysis of occupational exposure. *Microchem. J. 135*:1–9 (2017).

[47] **Ault, A.P., T.M. Peters, E.J. Sawvel, et al.**: Single-particle SEM-EDX analysis of iron-containing coarse particulate matter in an urban environment: Sources and distribution of iron within Cleveland, Ohio. *Environ. Sci. Technol. 46(8)*:4331–4339 (2012).

[48] **Friel, J.J., and C.E. Lyman**: X-ray mapping in electron-beam instruments. *Microsc. Microanal. 12(1)*:2–25 (2006).

[49] "Guide to casting and molding processes." Available at https://pdfs.semanticscholar.org/2fa7/9ad6d87450d1f12ff-b718ed58199b1bc7240.pdf (accessed May 9, 2018).

[50] **Loizaga, A., J. Sertucha, and R. Suarez**: Influence of treatments using different magnesium ferroalloys

on the melt quality and the solidification processes of ductile irons. *Rev. Metal. 44(5)*:432–446 (2008).

[51] **Lecoanet, H.F., J.Y. Bottero, and M.R. Wiesner**: Laboratory assessment of the mobility of nanomaterials in porous media. *Environ. Sci. Technol. 38(19)*:5164–5169 (2004).

[52] **Goudeli, E., M.L. Eggersdorfer, and S.E. Pratsinis**: Coagulation of agglomerates consisting of polydisperse primary particles. *Langmuir 32(36)*:9276–9285 (2016).

[53] **Goudeli, E., M.L. Eggersdorfer, and S.E. Pratsinis**: Coagulation-agglomeration of fractal-like particles: structure and self-preserving size distribution. *Langmuir 31(4)*:1320–1327 (2015).

[54] **Kim, S.C., J. Wang, M.S. Emery, W.G. Shin, G.W. Mulholland, and D.Y.H. Pui**: Structural property effect of nanoparticle sgglomerates on particle penetration through fibrous filter. *Aerosol Sci. Technol. 43(4)*:344–355 (2009).

[55] **Hofmann, W.**: Modelling inhaled particle deposition in the human lung—A review. *J. Aerosol Sci. 42(10)*:693–724 (2011).

[56] **Calmet, H., C. Kleinstreuer, G. Houzeaux, et al.**: Subject-variability effects on micron particle deposition in human nasal cavities. *J. Aerosol Sci. 115*: 12–28 (2018).

[57] **Tantra, R., J. Tompkins, and P. Quincey**: Characterisation of the de-agglomeration effects of bovine serum albumin on nanoparticles in aqueous suspension. *Colloids Surf. B. 75(1)*:275–281 (2010).

[58] **Ding, X., and F. Xie**: 3. Olfactory mucosa: composition, enzymatic localization, and metabolism. In *Handbook of Olfaction and Gustation*, R.L. Doty (ed.). Hoboken, NJ: John Wiley & Sons, Inc, 2015.

[59] **Cena, L.G., T.R. Anthony, and T.M. Peters**: A personal nanoparticle respiratory deposition (NRD) sampler. *Environ. Sci. Technol. 45(15)*: 6483–6490 (2011).

[60] **Byeon, J.H., J.H. Park, and J.H. Hwang**: Spark generation of monometallic and bimetallic aerosol nanoparticles. *J. Aerosol Sci. 39(10)*:888–896 (2008).

[61] **Therezien, M., A. Thill, and M.R. Wiesner**: Importance of heterogeneous aggregation for NP fate in natural and engineered systems. *Sci. Total Environ. 485*:309–318 (2014).

[62] **Hotze, E.M., J.Y. Bottero, and M.R. Wiesner**: Theoretical framework for nanoparticle reactivity as a function of aggregation state. *Langmuir 26(13)*:11170–11175 (2010).

[63] **Jassby, D., J.F. Budarz, and M. Wiesner**: Impact of aggregate size and structure on the photocatalytic properties of TiO2 and ZnO nanoparticles. *Environ. Sci. Technol. 46(13)*:6934–6941 (2012).

[64] **Pettibone, J.M., A. Adamcakova-Dodd, P.S. Thorne, P.T. O'Shaughnessy, J.A. Weydert, and V.H. Grassian**: Inflammatory response of mice following inhalation exposure to iron and copper nanoparticles. *Nanotoxicology 2(4)*:189–204 (2008).

[65] **Stebounova, L.V., N.I. Gonzalez-Pech, T.M. Peters, and V.H. Grassian**: Physicochemical properties of air discharge-generated manganese oxide nanoparticles: Comparison to welding fumes. *Environ. Sci.: Nano 5*:696–707 (2018).

[66] **Madl, A.K., and K.E. Pinkerton**: Health effects of inhaled engineered and incidental nanoparticles. *Crit. Rev. Toxicol. 39(8)*:629–658 (2009).

[67] **Adamcakova-Dodd, A., L.V. Stebounova, J.S. Kim, et al.**: Toxicity assessment of zinc oxide nanoparticles using sub-acute and sub-chronic murine inhalation models. *Part. Fibre Toxicol. 11*(*15*):1–15 (2014).

[68] **Park, J.H., I.A. Mudunkotuwa, J.S. Kim, et al.**: Physicochemical characterization of simulated welding fumes from a spark discharge system. *Aerosol Sci. Technol. 48(7)*:768–776 (2014).